

Opto-electronic properties of WS_2

Paweł Palczyński

August 24, 2018

Declaration

Acknowledgements

Abstract

List of abbreviations

List of figures

List of tables

1 Introduction

Following the discovery and characterisation of graphene in last decade the focus has been put on other 2D materials. Similar to graphene other bulk layered materials can exist in a monolayer or few layer form. Furthermore these thin layers also exhibit a significant change of properties when number of layers decreases from bulk all the way to monolayer. One of the most popular groups of these materials are transition metal dichalcogenides (TMDC). Their general form is MX_2 where M is a transition metal, and X is a chalcogen atom.

1.1 Properties of TMDCs

TMDCs in their layered form have been known, studied and utilised for a long time. They can be found commonly in use as solid-state lubricants or catalysts. About 60 different TMDCs have been studied and characterised with a general formula of X-M-X where a plane of metal atoms (M) is sandwiched between two chalcogen planes (X). Out of those 40 can be considered layered materials where individual layers are strongly bonded in-plane and weakly bonded out-of-plane in between layers. These weak, interlayer, Van der Waals interactions allow to form a bulk material. These bonds are also what allows for those layers to slide on top of one another similarly to other layered materials like graphite. TMDCs consist of two transition metal and single chalcogen atoms covalently bonded. They can be found in 3 distinct structural polytypes: 1T (tetragonal symmetry, octahedral coordination) with single layer per repeat unit, 2H (hexagonal symmetry,

trigonal prismatic coordination) with 2 layers per repeat unit and 3R (rhombohedral symmetry, trigonal prismatic coordination) with 3 layers per repeat unit [32] as can be seen in Figure 1.

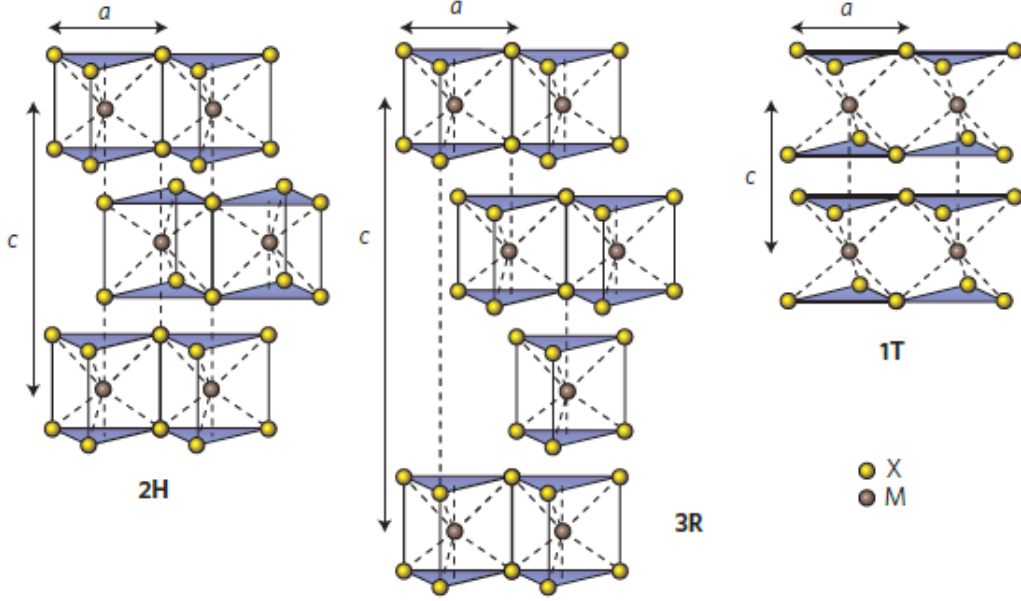


Figure 1: Schematics of the structural polytypes: 2H (hexagonal symmetry, two layers per repeat unit, trigonal prismatic coordination), 3R (rhombohedral symmetry, three layers per repeat unit, trigonal prismatic coordination) and 1T (tetragonal symmetry, one layer per repeat unit, octahedral coordination). The chalcogen atoms (X) are yellow and the metal atoms (M) are grey. The lattice constants a are in the range 3.1 to 3.7 Å for different materials. Adopted from [32]

Since graphene have proven to be difficult to work with in the fields of semiconductors due to its lack of natural finite electronic band gap its role as a successor in electronic and opto-electronic devices remains to be seen. However the techniques learned and effects observed during its characterisation were easily transferred to other layered compounds such as TMDCs. In particular the semiconducting, group VI-based TMDCs, containing sulphur and selenium as chalcogen atoms have proven to be more readily potentially useful as an active material in electronic and opto-electronic devices. This is due to their inherent electronic and optical bandgap in visible-near IR range.

As the number of layers changes from bulk to monolayer the properties of the TMDC undergo a significant change. In most TMDCs the bandgap changes from indirect to a larger direct one.

1.2 Electronic properties

One of the most interesting features that the layered TMDC materials exhibit is the shift in the bandstructure with the changing number of layers. Several studies have shown in simulations and experimentally that TMDCs have very similar electronic band structure as seen in example of WS_2 in Figure 2. In bulk WS_2 the maximum of the valence band (VBM) at Γ point and the minimum of the conduction band (CBM) at Λ form an indirect bandgap. As the number of the layers decreases the CBM at Λ point as well as VBM at K point increases causing the band gap to widen. At 2 layers the K point becomes the actual CBM and a new indirect bandgap forms between Γ point and K point. Finally in a WS_2 monolayer the VBM at K point as well as entire conduction

band increases to form a new greater direct band gap at K point. This means that WS_2 bandgap changes from 1.3 eV indirect bandgap in bulk to 2.1 eV direct bandgap in monolayer.

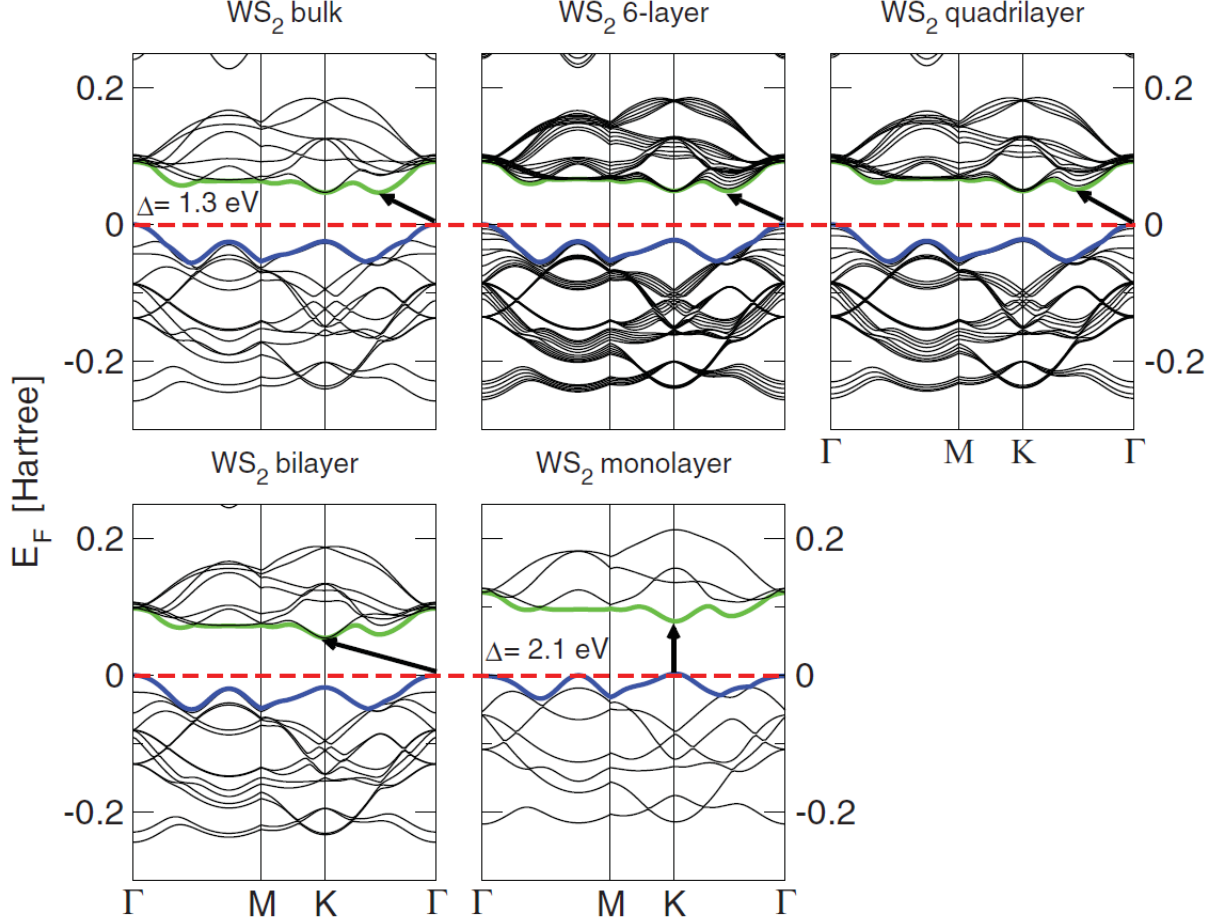


Figure 2: Band structures of bulk WS_2 , its monolayer, as well as, polylayers calculated from the density functional theory (DFT) simulation. The horizontal dashed lines indicate the Fermi level. The arrows indicate the fundamental band gap (direct or indirect) for a given system. The top of valence band (blue) and bottom of conduction band (green) are highlighted. Adopted from Ref. [17]

Like WS_2 other Mo and W based TMDC undergo similar transitions as seen in Table 1. In all cases the smaller indirect bandgap changes to greater direct bandgap with monolayer bandgap ranging from 1.1 eV to about 2.1 eV. Moreover the VBM at K points exhibits the orbit-spin band splitting at the K point of about 400 meV. This direct bandgap leads to presence of A and B excitons generated by transition between CBM and two VBMs at the K point. The conduction band as well as the valence band are dominated by the d-electron orbitals of the transition metal atoms and at the VBM and CBM they hybridize with the p-electron orbitals of the chalcogenide atoms. Because the hybridization happens mostly at the Γ point and the chalcogenide atoms are at the surface of the TMDC layer it leads to strong interactions between the layers. This leads to significant change in the band structure at the Γ and rise of the indirect bandgap as a result of increased number of layers. On the other hand at the K point the d-orbitals of the transition metals remain mostly unaffected due to them being positioned in the middle of the layer [17] [30]

Table 1: Mo and W based TMDC bandgaps comparison

M\X	$-S_2$	$-Se_2$	$-Te_2$
Mo	Semiconducting 1L: 1.8 eV Bulk: 1.2 eV	Semiconducting 1L: 1.5 eV Bulk: 1.1 eV	Semiconducting 1L: 1.1 eV Bulk: 1.0 eV
W	Semiconducting 1L: 2.1 eV Bulk: 1.4 eV	Semiconducting 1L: 1.7 eV Bulk: 1.2 eV	Semiconducting 1L: 1.1 eV

1.3 Optical properties

TMDCs exhibit a wide array of opto-electronic effects due to their strong light-matter effects. These effects are mostly caused by the abundant presence of excitons, bi-excitons, trions or bound excitons. As a result the change in layer thickness from bulk to monolayer alters the photoluminescence, photoconductivity and absorption in the visible to infrared range.

The primary and most common quasi-particle that forms in such system is an exciton, which is a pair of a negatively charged electron and a positively charged hole bound together by Coulomb forces to form a structure similar to that of hydrogen atom. Such pair is electrically neutral and is of size exceeding size of single cell which makes it a Wannier–Mott exciton. The recombination of these excitons results in a photon emission which can be easily observed during photoluminescence characterisation. On top of excitons other quasi-particles such as trions, bi-excitons or bound excitons can be found. A trion is a group of 2 electrons and a hole or 2 holes and an electron, or otherwise described as a charged exciton. The exact nature of the trion depends usually on the type of intrinsic doping of the TMDC. A bi-exciton is a pair of excitons which is usually only observed in quantum dot systems but can be also seen in excitonically dense systems such as TMDCs. A bound exciton is similar to the free exciton but is trapped by a defect. In a typical photoluminescence spectrum several peaks can be observed depending on specific type of TMDC characterised. In WS_2 monolayer for instance as seen in Figure. 3 the strongest peak (often labelled as an A peak) at about 1.97 eV is caused by the direct transition of single-photon generated exciton. Slightly redshifted by about 30 meV from the A peak a generally weaker peak caused by the trion recombination can be found. At higher energies another peak can be observed due to the presence of bi-excitons. At around the 1.3 eV a much weaker peak (I) can be seen caused by the indirect transition. Additionally a B peak can be observed blueshifted from the A peak which is caused by valley splitting as discussed in chapter 1.2. As seen in Figure 3 as the number of layers increases the main A peak becomes dramatically weaker due to lack of direct transition and redshifted following the pattern discussed in chapter 1.2. At the same time the I peak becomes relatively stronger and eventually dominates the bulk material.

Figure 3: Typical PL spectra of WS_2

Similarly the photoconductivity of the TMDCs is strongly reliant on the number of layers and incident photon energy. The MoS_2 for instance shows 3 times stronger photoconductivity in monolayer around 1.8 eV, where the direct transition is located, than in 2L MoS_2 around 1.6 eV.

Additionally the photoconductivity appears to increase in steps with relation to the photon energy following the direct and indirect transitions. [32].

The sunlight absorption in TMDCs has been shown to be significantly more intense than in commonly used solar cell materials, at about 5-10% which is an order of magnitude greater compared to similar thickness of Si or GaAs. It is also stronger compared to 2-3% of sunlight absorption of graphene. As a result a excitonic solar cell based on MoS_2/WS_2 bilayer shows about 1% power efficiency, about 3 times greater than that of typical ultrathin solar cells [2].

During standard single photon excitation photoluminescence studies the excitons generated can be called "bright" since they appear in PL spectrum. The reason we can observe them easily is because the spin between an electron and a hole is conserved, and thus allowing for photon emission. However another combination is possible, called dark exciton, where both electron and the hole have the same spin. Because of that they cannot recombine by emitting a photon and therefore remain absent from the PL spectrum. Even though they exist much longer than their bright counterparts their presence is of course also more difficult to observe. One way to observe them is to use two photon excitation. Due to two photon selection rule the single photon excitation can be excluded and the dark excitonic states can be observed. In WS_2 the dark excitons result in two peaks at 2.28 eV and 2.48 eV. [Probing excitonic dark states in single-layer tungsten disulphide]

Defect engineering allows to tune the number of charge carriers. In MoS_2 or WS_2 the sulfur vacancies lead to increased number of electrons in the material. Because of that by increasing the number of defects in those materials the level of n-doping can be changed. An easy way to observe the presence of those defects and subsequent quenching of them is to expose the material to varying amounts of oxygen, nitrogen or water. Due to greater electronegativity (???) those species attract the electrons and therefore the electron population in the material decreases. This in turn leads to smaller trion population since trions require an extra electron to form. This then can be observed in PL as a more narrow direct peak, with especially smaller redshifted shoulder. The effect can also be of course reversed by decreasing the amount of oxygen, nitrogen or water in the environment since those exist already in ambient conditions [Optical control of charged exciton states in tungsten disulfide].

In order to introduce and control the amount of vacancies in the TMDC different methods have to be explored. One of the ways of achieving that in already grown material is the use of oxygen plasma. It has been shown that the number of defects can be controlled by limiting the plasma exposure. During the process the oxygen also chemically bonds to the MoS_2 at the defect sites and therefore partially negates the effect of defects on the optical properties. The PL can also be seen to increase in intensity with increasing number of defects with oxygen adsorbed due to the increased yield of bound excitons localised at these defects. [Strong Photoluminescence Enhancement of MoS_2 through Defect Engineering and Oxygen Bonding]

Similar effect has been shown using the 2,3,5,6-tetrafluoro-7,7,8,8-tetracyanoquinodimethane (F_4TCNQ), 7,7,8,8-tetracyanoquinodimethane ($TCNQ$) and (nicotinamide adenine dinucleotide) $NADH$ for chemical doping. Both F_4TCNQ and $TCNQ$ are p-type dopants while $NADH$ is a n-type dopant. By exposing the surface of MoS_2 to these compounds the change in PL intensity and FWHM have been observed. Similar to doping with O_2 , N_2 or H_2O , all of which are p-type dopants, the intensity of PL has increased in presence of F_4TCNQ and $TCNQ$. The effect has been similarly ascribed to lowering the number of defects and therefore the lowering the trion population and subsequently increasing the exciton population increasing the yield. The opposite observation has been made with use of $NADH$ with PL intensity decreasing. Similarly the increase in trion population with lower PL yield is ascribed to the lower PL intensity. [Tunable Photoluminescence of Monolayer MoS_2 via Chemical Doping].

It has also been shown that alloying can be used to fine tune the PL by varying the concentration of alloying material. In monolayer $Mo_{1-x}W_xS_2$ the PL peak position initially decreases from 1.575 eV (PL peak position of pure MoS₂) to 1.56 eV at $x=0.21$ and then increase up to 1.65 eV (PL peak position of WSe₂) at $x = 1$. This effect could be attributed to the linearity of VB and non-linearity of CB with regards to change in W composition. The PL position can therefore be engineered on a monotonic range from 1.56 eV to 1.65 eV. In bilayer $Mo_{1-x}W_xS_2$ alloy the position of both direct and indirect transition PL peaks increases monotonically from about 1.49 eV and 1.53 eV for pure MoSe₂ to 1.56 eV and 1.62 eV for pure WSe₂ as the W amount is increased. This opens another relatively easy way of engineering PL position [Two-Dimensional Molybdenum Tungsten Diselenide Alloys: Photoluminescence, Raman Scattering, and Electrical Transport].

Another effect that has been demonstrated that allows for certain degree of control of PL in TMDCs is relation between the helicity of incident light and valley population valley population. It has been shown that by exciting the monolayer MoS_2 with right-polarised light the resulting excitons will fill primarily the VB at K point. Similarly by exciting the MoS_2 with left-polarised light the excitons will fill the VB at K' point. After recombination the resulting photons will exhibit the same circular polarity as the photons that excited the electrons in the first place. [Tightly bound trions in monolayer MoS₂] [Control of valley polarization in monolayer MoS₂ by optical helicity]

The temperature effect on TMDCs has also been investigated. In WSe_2 monolayer it has been shown that as the temperature of the sample increases from room temperature to about 400K the position of the direct transition PL peak redshifts from about 1.65 eV to about 1.58 eV. When the temperature is decreased from room temperature to about 5K the same peak blueshifts to about 1.7 eV. Between 100K and 50K as well 20K and 5K the position of the PL peak does not change. Additionally around 120K another peak appears and as the temperature is lowered it also blueshifts although less than the RT peak. The peak only present at RT is attributed to free excitons whereas the peak appearing at 120K is ascribed to bound excitons. As bound exciton peak appears its intensity increases with lower temperature while the intensity of the free exciton peak decreases. This indicates that the population of free excitons decreases while the population of the bound excitons increases with decreasing temperature [31]

There has been many reports on the spatial distribution of PL in the TMDCs. One of the observed patterns in WS₂ and MoS₂ has been that of much stronger PL intensity at the edges of the flakes. That effect has been primarily observed in small flakes of about 5 μm [11].

1.4 Phonon dispersion

The vibrational and phononic characteristics of TMDCs have been investigated at length by both theoretical simulations as well as experimental studies. The $2H - MX_2$ crystal structure of the TMDCs belongs to D_{6h}^4 point group and there are 18 lattice dynamical modes at the Γ point. Phonons belonging to these modes can be represented as Eq. 1 [33]:

$$\Gamma = A_{1g} + 2A_{2u} + B_{1u} + 2B_{2g} + E_{1g} + 2E_{1u} + E_{2u} + 2E_{2g} \quad (1)$$

In TMDCs 4 active Raman modes can be observed $E_{1g}, E_{2g}^1, E_{2g}^2, A_{1g}$. These can be seen in Figure 4. The E_{2g}^2 is a shear mode that involves 2 layers vibrating against each other. The E_{1g} is an in-plane vibration of chalcogen atoms but is forbidden in the back-scattering configuration. For monolayers therefore it leaves primarily the E_{2g}^1 which is an in-plane mode involving vibration of both metal and chalcogen atoms as well as A_{1g} which is an out-of-plane mode involving only chalcogen atoms.

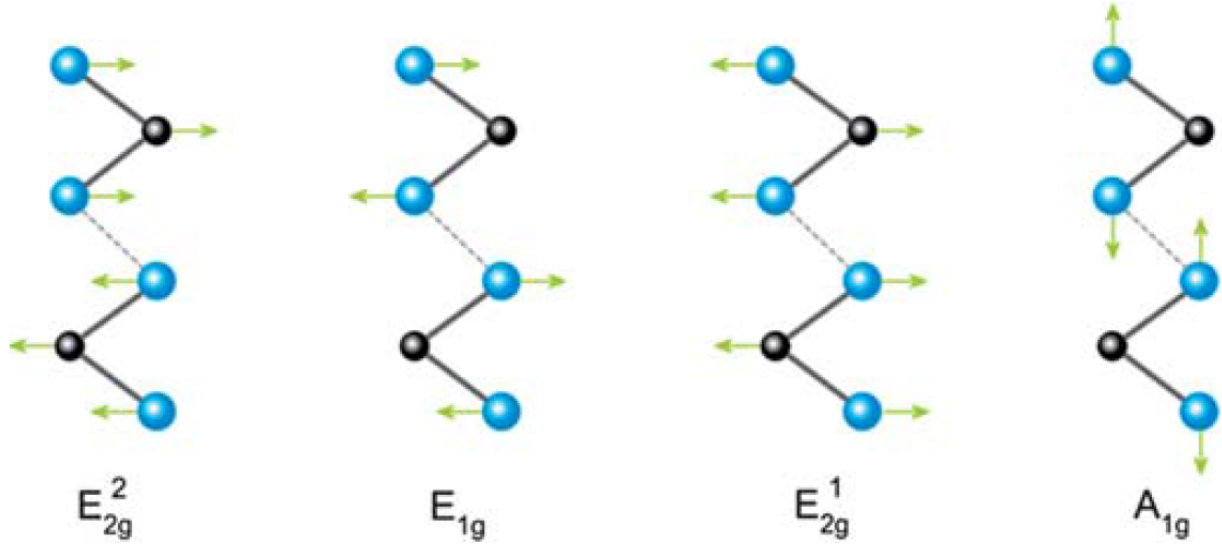


Figure 4: 4 active Raman modes in TMDCs. Metal atoms and chalcogen atoms are black and blue respectively. Adopted from [33]

These two peaks tend to dominate the spectrum of any TMDCs, whether monolayer or few-layer or bulk. The shear mode E_{2g}^2 appears at low Raman shift frequencies and is therefore difficult to observe but can be used to differentiate monolayer from few-layer material. Since E_{2g}^1 is an in-plane mode it tends to be unaffected by the number of layers due to weak van der Waals forces between the layers but can be seen to be slightly redshifted as the number of layers increases. As seen in Figure 5 the E_{2g}^1 peak at about 352 cm^{-1} is overlapping with another stronger peak, a 2LA(M) peak at 350 cm^{-1} which is a longitudinal acoustic mode caused by in-plane collective oscillations of W and S atoms. The second strongest peak at around 416 cm^{-1} is an A_{1g} peak, caused by out of plane vibrations. Because of that it is much more sensitive to the number of layers and is seen to become blueshifted as the number of layers increases. This has been attributed to the restorative forces as well as increase in dielectric screening of the Coulomb forces. Combining both of these shifts in frequency with the changing number of layers the difference between these two peak position can be used to identify the number of layers in TMDCs as seen in Figure 6

Figure 5: Typical Raman spectrum of WS_2

Figure 6: Identification of number of layers by the difference in position of A_{1g} and E_{2g}^1 peaks.

1.5 Heterostructures

1.6 Applications

2 Methods

2.1 Raman spectroscopy theory

2.2 Photoluminescence spectroscopy theory

2.3 XPS theory

3 Role of precursors in growth of monolayer WS_2

3.1 Introduction

Monolayers of transition metal sulphides and selenides exhibit range of interesting properties such as strong light absorption in the IR and visible range [25][2][42], valley polarisation [24] [13], spin-orbit interactions [36][43], tightly bound excitons [23] or second-harmonic generation [21]. Some of these effects can be attributed to the lack of free dangling bonds and configuration of d-orbitals [34], [20].

Among these materials one of the most promising is the WS_2 . Its visible range bandgap of 2eV as well as an easy and safe manufacturing route via CVD makes it one of the more interesting and studied TMDCs. The typical characterisation by photoluminescence spectroscopy allows to probe the varying synthesis conditions, the grain boundaries or defect population [11] [27] [19] [28]. The PL efficiency in as-grown monolayer WS_2 produced via CVD growth shows ~ 2 -6% efficiency [27][38] [22]. This efficiency is caused mostly by defect-mediated non-radiative recombination centres [1]. LEDs have been successfully produced [15] showing external quantum efficiency up to 10% [40][35]. WS_2 is typically a n-type semiconductor due to the presence of sulphur vacancies [11][29][14]. In order to utilise this material in any potential future applications a reliable and scalable manufacturing method must be developed to ensure a high quality crystal on the wafer scale area. The main method for WS_2 synthesis that satisfies these conditions is Chemical Vapour Deposition (CVD) [12]. The growth of tungsten based TMDCs have been less successful than the equivalent molybdenum based TMDCs and has produced mostly isolated flakes of up to 40 μm [11] [41] [28] [6][37][7][18]. Even larger films of monolayer WS_2 have been shown, however they also exhibit low carrier mobility [16][8]. In the typical CVD synthesis process the sulphur and tungsten oxide are evaporated simultaneously in a tubular furnace with a constant flow of carrier gas like argon at temperatures of at least 900 $^{\circ}C$ [11][41][28][6][37][7][18]. Such growth is predicated by topotactic transformation leading to low density distribution of domains on an amorphous [11][41][6][7][18] or crystalline substrate [28][37][26] possibly due to low evaporation rates of WO_3 . Since WO_3 requires high temperatures of 950-1000 $^{\circ}C$ to evaporate while the S becomes volatile at 90 $^{\circ}C$ the thermodynamics of the process are difficult to control. The low growth dictated by fast evaporation of S leads to limited domain growth and lack of continuous layer. One of the proposed solutions have been to spread the WO_3 on the target substrate [27][19][8][4][39][10][9]. This has however led to low reproducibility, poor control of thickness and stoichiometry and unreacted material left on the substrate. Another approach has been to use more volatile W precursors such as WCl_6 [3] or $W(CO)_6$ [16][5] together with organic compounds as S precursors. Such method

while producing a large area domains at lower temperature has led to lower crystal quality and purity.

Here we propose a different method of CVD synthesis that allows for much larger flake growth of up to $800\ \mu\text{m}$ at temperature of $750\ \text{degreeC}$. Such grown material exhibits high electron mobility in one and two layers of WS_2 , higher than other values reported in literature. The photoluminescence peak is also very narrow at $36\ \text{meV}$ FWHM at room temperature.

3.2 Results

For the purpose of comparing the CVD synthesis method conditions the several sets of precursors were used: WO_3 , $WO_3 + NaCl$ and $H_2WO_4 + NaCl$.

RESULTS The synthesis of WS_2 was performed starting from commercial powders of H_2WO_4 , WO_3 , S and where indicated, we have introduced $NaCl$. W and S precursors were placed in two separate crucibles well-spaced in a quartz tubular furnace (Supplementary Information, Figure S1a) and heated up independently using different controllers as reported in Figure S1b. The heating profile of S has been optimized to ensure maximum supply when the W-precursors start evaporating. SiO_2 ($285\ \text{nm}$)/Si substrates were utilized for the growth and loaded in the downstream zone of the tubular furnace. This approach allows for a controllable and reproducible large-area deposition of uniform WS_2 domains compared to placing the substrate above the metal precursor crucible. The syntheses were carried out under low vacuum and a flux of Ar gas. Optical micrographs of WS_2 monolayers (Figure 1) grown by using different W precursors (WO_3 , WO_3 - $NaCl$ and H_2WO_4 - $NaCl$) at different temperatures ($950\ ^\circ\text{C}$, $850\ ^\circ\text{C}$ and $750\ ^\circ\text{C}$) show distinctively increasing lateral size of the triangles and increasingly facilitated synthesis at lower temperatures from the left to the right side of the figure. For all of the growth conditions, we observe that the WS_2 triangles present sharp edges and uniform colour contrast onto SiO_2 , suggesting formation of pristine monolayer WS_2 across the entire triangle area. WO_3 precursor growth leads to monolayered WS_2 triangles with lateral size of $\sim 10\ \mu\text{m}$ at $950\ ^\circ\text{C}$ (Figure 1a) while no deposition of WS_2 is observed at lower temperatures ($850\ ^\circ\text{C}$ and $750\ ^\circ\text{C}$) (Figure 1b, c). The fact that the synthesis can occur only at very high temperature is explained by the high sublimation temperature of WO_3 .

Figure 1 Optical micrographs of WS_2 triangles grown on SiO_2 /Si substrates at different temperatures and using different precursors: (a) WO_3 at $950\ ^\circ\text{C}$; (b) WO_3 at $850\ ^\circ\text{C}$; (c) WO_3 at $750\ ^\circ\text{C}$; (d) WO_3 and $NaCl$ at $950\ ^\circ\text{C}$; (e) WO_3 + $NaCl$ at $850\ ^\circ\text{C}$; (f) $WO_3 + NaCl$ at $750\ ^\circ\text{C}$, the OM appears as a bare SiO_2 substrate; (g) $H_2WO_4 + NaCl$ at $950\ ^\circ\text{C}$; (h) H_2WO_4 and $NaCl$ at $850\ ^\circ\text{C}$; (i) $H_2WO_4 + NaCl$ at $750\ ^\circ\text{C}$.

The WO_3 + $NaCl$ system overall facilitates the synthesis of WS_2 triangles leading to $\sim 60\ \mu\text{m}$ flakes at $950\ ^\circ\text{C}$ (Figure 1d) and $\sim 30\ \mu\text{m}$ (Figure 1e) at $850\ ^\circ\text{C}$. The larger WS_2 domains obtained at higher temperatures can be explained in the light of the Robinson & Robin model []. At high temperature the diffusivity of the adsorbed precursors on the SiO_2 surface is favourable leading to the expansion of the existing domains. At the same time the desorption of absorbed species is higher than at lower temperatures, limiting the achievement of a supersaturation concentration and thus reducing the nucleation density. By further lowering the growth temperature to $750\ ^\circ\text{C}$, no WS_2 domains have been observed (Figure 1f) likely due to the insufficient evaporation of WO_3 . By replacing WO_3 with H_2WO_4 the lateral size of the WS_2 monolayered domains significantly increases (Figure 1g,h,i). The triangular crystals have edge lengths exceeding $200\ \mu\text{m}$ at temperatures higher than $850\ ^\circ\text{C}$ and between 50 - $200\ \mu\text{m}$ at $750\ ^\circ\text{C}$ (Figure 1g,h,i). Continuous polycrystalline monolayer coverage has been obtained over areas of $\sim 0.8\ \text{mm}$ extension (Figure S2). Increasing the growth pressure (from $1.6\ \text{mbar}$ to $13\ \text{mbar}$) at $950\ ^\circ\text{C}$ bilayered WS_2

flakes are preferentially formed (Figure S3). To understand the facilitated synthesis of WS₂ using H₂WO₄ and NaCl, we conducted X-ray diffraction (XRD) analysis of the reaction products between H₂WO₄+NaCl and WO₃+NaCl systems at different temperatures (500 °C, 650 °C and 750 °C) to understand the chemical differences (Figure S4). We found that the main products of the reactions between NaCl and H₂WO₄ are: Na_xWyO_z and tungsten oxychloride (WClO₄ and WO₂Cl₂). The Na_xWyO_z possesses a high evaporation temperature as it remains in the crucible (Figure S5) after the synthesis of WS₂ is completed. Further, using this compound as precursors for a new growth of WS₂ at 950 °C did not lead to the formation of any WS₂ flakes, confirming the high evaporation temperature. On the bases of previous studies on the synthesis of bulk crystals, the formation of tungsten oxychloride species (WO₂Cl₂ and/or WOCl₄) is likely to occur while the formation of metal halides is less favourable (e.g. WCl₆) []. Tungsten oxychlorides are volatile already at 200 °C [] and they can be sulfidized in vapour phase and then be deposited onto the target substrate as atomic clusters. WOCl₄ has been previously used [43] as precursor for the CVD synthesis of WS₂ bulk films. Despite its strong tungsten oxygen double bonds, WOCl₄ proved to be an effective precursor with a clean decomposition pathway in the CVD process without formation of tungsten oxysulfide. We have verified that using this precursor is indeed possible to obtain WS₂ at temperatures as low as 550 °C (Figure S6a). The key role played by the oxyhalide species it becomes apparent if we try to grow WS₂ by using only hydrated tungsten oxide. As this decomposes to form WO₃, only small WS₂ domains are observed with similar PL characteristics to the WO₃ precursors-growth (Figure S6b). Furthermore, to confirm the key role played by Cl, we replaced NaCl with KCl and we obtained comparable growth results (Figure S6c). High resolution TEM imaging confirms the pure crystalline nature of the material (Figure 2a). The measured lattice constant is 0.3 nm consistent with that of 2H-WS₂ (a=0.318 nm). The AFM thickness profile analysis of WS₂ triangles confirms the monolayer (Figure 2b,c) and bilayer (Figure S3d,e) nature of the flakes. This shows an edge step height of ~0.8 nm which confirms the monolayer nature of the WS₂ domains []. The Raman spectra of WS₂ obtained under the different growth conditions are shown in Figure 2d. All of the spectra exhibit two characteristic peaks located at ~(351±0.53) cm⁻¹ and ~(417.6±1) cm⁻¹, which can be attributed to 2LA-E12g and A1g Raman modes of pristine WS₂ monolayer []. Interestingly the distribution of the peak positions is increasingly narrower going from WO₃ precursor, to WO₃+NaCl and to H₂WO₄+NaCl (Figure S8, S10). The Raman peak intensities are uniform across the entire triangle area (Figure S7, S9) and the energy difference ($\Delta\nu$) between 2LA(M) and A1g is ~(66.5±0.53) cm⁻¹ (Figure S11), as expected for WS₂ monolayers [51].

Figure 2 Structural and physical characterization of WS₂ triangles: (a) HRTEM image of the WS₂ lattice grown using H₂WO₄+NaCl, the inset report a selected diffraction area which show a hexagonal pattern. (b) Raman spectra showing the characteristics active modes of WS₂ grown under different conditions and compared with mechanically exfoliated flakes. (c) AFM image and (d) corresponding thickness profile of monolayer WS₂. A comparison of representative photoluminescence (PL) intensity maps of WS₂ monolayers grown by using the three precursor systems at different temperatures is reported in Figure 3. The PL intensity map of WS₂ monolayers grown at 950 °C from WO₃ (Figure 3a) shows a three-lobes intensity pattern. The PL spectra appear asymmetric and they can be deconvolved in two distinct peaks which have been attributed to an exciton and a trion component (Figure 4a) []. The PL peak positions of the same WS₂ flake show a bimodal distribution with areas with high PL intensity distributed over three lobes characterized by a peak position distribution centred at 1.94 eV versus areas with low intensity and peak position centred at 1.96 eV. The FWHM is centred at 75 meV versus 55 meV respectively in the two areas (Figure 4a-c) (Figure S12, S13, S15). Peak position and FWHM are comparable

with the current state-of-the-art of WS₂ synthesis from WO₃ [4][18][]]. The red shift of ~ 0.02 eV of the peak position (Figure 4b) and the larger FWHM (Figure 4c) of the three-lobe areas suggests higher concentration of structural defects [][59]. In particular in the form of S-vacancies which increases the electron density and consequently the trion population [4][]. This leads to the strengthening of PL emission at lower energies than the optical band gap (Figure 4) causing a redshift and an increased FWHM of the peak [4][57]. Strain variations in the lattice can also affect the light emission intensity and wavelength [][]. To prove whether lattice strain could affect the PL energy and the intensity variation, we have relaxed the lattice by cutting the WS₂ domain using a high intensity 532 nm laser. As reported in Figure S14, the PL peak intensity and energy position patterns remain unchanged along with the Raman peak position. Thus, structural defects in variable concentration are likely to be the main responsible for the PL intensity and peak position pattern []. The samples grown with the addition of NaCl present light emission at higher energy and FWHM narrower compared to the WO₃-led growth. The PL spectra appear asymmetric and they can be deconvolved in two distinct peaks which have been attributed to an exciton and a trion component (Figure 4a). The distribution of the PL peak position and FWHM is uniform within the same triangle but bimodal with respect to different triangles and they possess small standard deviations (Figure 4b-c) (Figure S12, S13, S16) compared to the WO₃-led growth. The light emitted has higher energy ($\sim 1.95 \pm 0.002$ eV and 1.96 ± 0.002 eV) and the FWHM of the peaks is narrower ($\sim 43 \pm 2.8$ meV and 51 ± 3 meV) (Figure 4), compared to WO₃-led growths and most of the reported works [4][18][54][55]. This suggests that the trions component is now reduced. Thus we can conclude that WS₂ grown from NaCl+WO₃ is affected by less structural defects compared with WO₃-growth. A different growth dynamics (topotactic versus molecular conversion) which leads to a different distribution of defects can explain the differences observed (Figure 3b-c).

Figure 3 Spatial maps of PL intensity of WS₂ grown in the conditions exemplified in Figure 1. The scale bar length is $10 \mu\text{m}$. The overall PL peak intensity of WS₂ monolayers (Figure 3d-f) grown using H₂WO₄+NaCl is considerably higher compared to the previously discussed growth systems. Further, the FWHM is significantly narrower ($\sim 36 \pm 3$ meV), and the PL energy ($\sim 1.980 \pm 0.005$ eV) is higher compared to FWHM and emitted light observed for WS₂ grown under WO₃ and WO₃+NaCl precursors (Figure 4) (Figure S12, S13, S17). This suggests that the material grown by using H₂WO₄+NaCl possess even less structural defects and particularly in the form of sulfur vacancies, which lead to a negligible contribution from trions (Figure 4a). Further, no appreciable differences are observed from flake to flake, confirming the high reproducibility of the process. The FWHM is smaller than previously reported values for CVD-grown [4][18][54][55] and exfoliated WS₂ [6][] (Figure 4a) while it is comparable to WS₂ grown on van der Waals substrates [38] and to high quality exfoliated WS₂ [22]. Overall the distribution of the PL peak position and the FWHM for the samples grown introducing H₂WO₄ are much narrower (5 meV and 3 meV respectively) (Figure S18) compared with the other precursors results. Different intensity patterns across individual flakes can still be recognized, however, they present smaller intensity difference compare to the other growth conditions.

Figure 4: PL spectra characteristics of WS₂ grown using: WO₃ at 950 °C, WO₃+NaCl at 850 °C, H₂WO₄+NaCl at 850 °C: (a) individual spectra (dotted line) and deconvolution in exciton and trion components; (b) distribution of PL peak position and (c) distribution of PL FWHM for several WS₂ grown using the three different precursor systems. XPS characterization confirms the greater efficiency of tungstic acid in inducing a complete sulfidization of the precursors compared with the WO₃+NaCl system. Analysing WS₂ grown using H₂WO₄+NaCl, the W 4f_{5/2} and W 4f_{7/2} core levels (Figure 5a) present peak position characteristic of W⁴⁺ in WS₂ [][] (32.7 and

34.8 eV respectively) and the narrowest achievable FWHM (1 eV) (Figure 5a), using the Mg $K\alpha$ as X-ray source. This indicates chemical purity and perfect stoichiometric ratio of W and S. This has been also confirmed by calculating the concentration of S and W from the integrated intensity of the W 4f and S 2p core levels. The S 2p_{1/2} and 2p_{3/2} core levels, also appear at the expected position for WS₂ (162.3 eV and 163.4 eV respectively, Figure 5b) [63] and with a very narrow FWHM (1 eV) (Figure 5c). A very small amount of W₆₊ (W 4f_{5/2} and W 4f_{7/2} core levels centred at 35.9 eV and 38.1 eV respectively in Figure 5a) attributable to WO₃, which partially overlaps with the W 5p core level (38.5 eV), can be observed which however disappears after transferring the flakes on a new SiO₂/Si substrate (Figure 5c) and thus suggesting that it is related to residual precursors on the substrate considering the XPS spot size is ~ 1 mm. It is worth noting that after transfer the FWHM of the W 4f core levels remains unchanged suggesting that the transfer process preserves the crystallinity of the flakes and no additional defects are introduced. Similarly, chemical purity and expected stoichiometric ratio of 2:1 for S:W have been observed for WS₂ grown from WO₃+NaCl (Figure 5a). Nevertheless, a larger W₆₊ contribution, attributable to WO₃ (W 4f_{5/2} and W 4f_{7/2} centred at 35.9 eV and 38.1 eV respectively in Fig 5a) has been detected in this case suggesting that a conspicuous amount of precursors does not get sulfurized and it is just deposited onto the SiO₂ wafer. Upon transfer on a new SiO₂/Si substrate, this component entirely disappears (Figure 5c), thus indicating also in this case that WO₃ is mainly distributed on the substrate. The FWHM of the W₄₊ 4f core levels is ~ 1.2 eV in this case, suggesting higher concentration of defects compare to H₂WO₄+NaCl-led growth (Figure 5a). The transferred WS₂ present a FWHM even larger ~ 1.3 eV, suggesting the introduction of atomic defects as a consequence of the mechanical stress underwent by the flakes (Figure 5c). To conclude, XPS study confirms the effectiveness of H₂WO₄ as precursor versus WO₃.

Figure 5 XPS spectra of the W 4f and S 2p core level peak regions. (a) Comparison of W 4f_{5/2}, W 4f_{7/2} and W 5p core levels of WS₂ grown using H₂WO₄+NaCl at 950 °C (blue spectrum) with WS₂ grown using WO₃+NaCl at 950 °C (red spectrum). The deconvolution of W 4f_{5/2}, W 4f_{7/2} and W 5p core levels and overall fit of the spectrum are reported as black dashed and a continuous line respectively. (b) The S 2p_{1/2} and 2p_{3/2} core levels for each of the two growth conditions are reported in the central panel. (c) W 4f_{5/2}, W 4f_{7/2} and W 5p core levels before (dashed line) and after transfer (continuous like) onto a new SiO₂/Si substrate are compared showing the complete disappearance of the residual WO₃ components. The spectra were fit by Doniach-Sunjc function after subtracting a Shirley background (black dashed line). The progressive reduction of structural defects from using WO₃ to H₂WO₄ has been proven by electrical characterization. The electrical properties of the WS₂ were characterised through their performance in bottom-gated field effect transistors (Figure 6a,b). The FET transfer curve (Figure 6c), displays an accumulation-type n-channel transistor, where the current flowing through the channel increases with increased gate bias, after the threshold voltage. The gate bias range was extended up to the point at which the channel current reached a linear regime, characterised by $I_d = \mu_n C_{ox} (W/L) ((V_{gs} - V_{th}) V_{ds})$, where μ_n is the electron field-effect mobility, C_{ox} is the oxide dielectric and V_{th} is the threshold voltage. The typical response curves (Figure 6d) at different gate biases for a WS₂ triangle grown using H₂WO₄ and transferred onto a fresh SiO₂ substrate exhibit asymmetry about $V_{ds} = 0$ V which originates from the different electrostatic potential seen at the source and drain electrodes. While the Schottky barrier at the source electrode is pinned by the gate, the drain barrier decreases with negative drain bias, and vice versa. However, as the semiconductor bands become more bent at the semiconductor/metal interface with increasing gate bias, the contribution of tunnelling currents through the barrier becomes more significant and as a result, the contacts become more “Ohmic” in nature.

Figure 6 Electrical characteristics of monolayer WS₂: (a) Schematic of the bottom-gated field effect transistors; (b) optical micrograph of the device (scale bar is 20 μm); (c) FET transfer curve for the monolayer WS₂ grown using H₂WO₄+NaCl at 950 °C showing the highest mobility of 28 cm²/Vs (linear region of the transport graph marked with a red-dashed line); (d) Response curves at different gate biases for a WS₂ triangle grown using H₂WO₄+NaCl; (e) FET transfer curve for the monolayer WS₂ grown using WO₃+NaCl at 800 °C; (f) electron mobilities of monolayer WS₂ grown using different conditions. The field-effect mobility was calculated in the linear region of the transport graph (marked with red-dashed line in Figure 6c), using $\mu_n = C_{ox}^{-1}(d\sigma/dV_{gs})$. Overall, monolayer WS₂ grown using H₂WO₄+NaCl show electron mobilities systematically higher compared with the WO₃+NaCl system (Figure 6c,d,e,f) corroborating the higher crystal quality expected by using H₂WO₄ as precursors. Further, monolayer WS₂ presents electron mobility of 28cm²/Vs (Figure 6c,f) which is the highest mobility reported so far for CVD grown WS₂ and deposited onto SiO₂ (Figure 7a) [17][30][31][32][34][36][40][] [] [] and comparable to mechanically exfoliated WS₂ [51][] [] [71]. The highest mobilities using either H₂WO₄+NaCl or WO₃+NaCl precursor systems, are displayed by WS₂ grown at 950 degreeC (Figure 6f) suggesting that the growth temperature does also play a role in improving the crystal quality of the material without inducing S desorption. The role played by the different precursor system in determining the crystallinity of the materials becomes more prominent lowering the growth temperature. WS₂ grown with the H₂WO₄+NaCl precursors system leads to electron mobilities comprised between 10 and 20 cm²/Vs at temperatures between 750 degreeC and 850 degreeC. While the electron mobilities of WS₂ grown using WO₃+NaCl (Figure 6f) display much lower values \sim 2 cm²/Vs (at 800 \sim C). Bilayered WS₂ triangles show electron mobility systematically higher than monolayer (between \sim 38 cm²/Vs and 52 cm²/Vs) (Figure 8), as also observed for mechanically exfoliated flakes [] []. The electron mobility of 52 cm²/Vs (Figure 7b and Figure 8) is higher than CVD grown WS₂ as well as mechanically exfoliated sheets WS₂ onto SiO₂ reported so far [26][70][71]. The fact that the highest mobility for bilayer WS₂ has been obtained using WO₃+NaCl precuros system withouth the use of H₂WO₄ suggests that the bilayer system, which present much higher mobilities than single layer is less affected by the precursos choice, and once a bilayer material has been obtained already present crystal quality that stand above any monolayer system.

Figure 7 Comparison of our results with the literature of CVD grown material and mechanically exfoliated WS₂ (MEX) : electron mobility for (a) monolayer WS₂ and (b) bilayer WS₂. The histograms show our record values for both monolayer and bilayer amongst the best values reported for CVD grown WS₂.

Figure 8 Electrical characteristics of bilayer WS₂: (a) Optical micrograph of the device (scale bar is 30 μm); (b) FET transfer curve for the bilayer WS₂ grown using WO₃+NaCl at 950 °C showing the highest mobility of 52 cm²/Vs (linear region of the transport graph marked with a red-dashed line); (c) electron mobility of bilayer WS₂ grown by using different precursor systems.

CONCLUSIONS In conclusion, we have developed a synthesis strategy, which enables high crystal quality WS₂ as reflected in the high optical quality and in the carrier mobility that overcome naturally occurring materials. The molecular precursors approach leads to effective sulfidization of W, revealing to be highly advantageous with respect to the traditional oxide-based conversion synthesis of WS₂. These results can be translated and applied to the synthesis of different TMDs, and pave the way towards industrially scalable synthesis of monolayer WS₂ over large areas.

4 Characterisation of WS_2

4.1 Optical microscopy of WS_2 flakes

4.2 Raman spectroscopy of WS_2

4.2.1 Interlayer interactions

4.2.2 Strain

4.2.3 Grain boundaries

4.3 Photoluminescence spectroscopy

4.3.1 PL of WS_2 monolayer

4.3.2 PL variation vs flake size

4.3.3 PL variation vs synthesis conditions

4.3.4 Spatial PL variation

4.3.5 Effects of water and oxygen on PL

5 Transfer of mono- and fewlayer WS_2

5.1 Motivation

5.2 Wet transfer

5.2.1 Methods

5.2.2 Effects on optical and electronic properties

5.3 Dry transfer

5.3.1 Methods

5.3.2 Effects on optical and electronic properties

6 Low temperature characterisation of WS_2

6.1 Setup

6.2 Isolating trions and excitons

6.3 Spatial variation of PL

7 In doped WS_2

7.1 Doping theory

7.2 Quantifying In doping

7.3 Effects of doping on PL

7.4 Effects of doping on Raman spectroscopy

F. M. Pesci *et al.*, "MoS₂/WS₂ heterojunction for photoelectrochemical water oxidation", ACS Catalysis, 2017 - accepted

Conferences

Graphene Week, 13-17 June, 2016. (Best poster)

UK Semiconductors, 14-15 July, 2017.

MRS Boston, 26 November - 1 December, 2017.

References

- [1] M. Amani, D.-H. Lien, D. Kiriya, J. Xiao, A. Azcatl, J. Noh, S. R. Madhupathy, R. Ad-dou, S. KC, M. Dubey, K. Cho, R. M. Wallace, S.-C. Lee, J.-H. He, J. W. Ager, X. Zhang, E. Yablonovitch, and A. Javey. Near-unity photoluminescence quantum yield in MoS₂. *Science*, 350(6264):1065–1068, nov 2015.
- [2] Marco Bernardi, Maurizia Palummo, and Jeffrey C. Grossman. Extraordinary sunlight absorption and one nanometer thick photovoltaics using two-dimensional monolayer materials. *Nano Letters*, 13(8):3664–3670, Aug 2013.
- [3] Claire J. Carmalt, Ivan P. Parkin, and Emily S. Peters. Atmospheric pressure chemical vapour deposition of WS₂ thin films on glass. *Polyhedron*, 22(11):1499–1505, jun 2003.
- [4] Chunxiao Cong, Jingzhi Shang, Xing Wu, Bingchen Cao, Namphung Peimyoo, Caiyu Qiu, Litao Sun, and Ting Yu. Synthesis and optical properties of large-area single-crystalline 2d semiconductor WS₂ monolayer from chemical vapor deposition. *Advanced Optical Materials*, 2(2):131–136, dec 2013.
- [5] Sarah M. Eichfeld, Lorraine Hossain, Yu-Chuan Lin, Aleksander F. Piasecki, Benjamin Kupp, A. Glen Birdwell, Robert A. Burke, Ning Lu, Xin Peng, Jie Li, Angelica Azcatl, Stephen McDonnell, Robert M. Wallace, Moon J. Kim, Theresa S. Mayer, Joan M. Redwing, and Joshua A. Robinson. Highly scalable, atomically thin WSe₂ grown via metal–organic chemical vapor deposition. *ACS Nano*, 9(2):2080–2087, feb 2015.
- [6] Ana Laura Elías, Néstor Perea-López, Andrés Castro-Beltrán, Ayse Berkdemir, Ruitao Lv, Simin Feng, Aaron D. Long, Takuya Hayashi, Yoong Ahm Kim, Morinobu Endo, Humberto R. Gutiérrez, Nihar R. Pradhan, Luis Balicas, Thomas E. Mallouk, Florentino López-Urías, Humberto Terrones, and Mauricio Terrones. Controlled synthesis and transfer of large-area ws₂ sheets: From single layer to few layers. *ACS Nano*, 7(6):5235–5242, 2013. PMID: 23647141.
- [7] Qi Fu, Wenhui Wang, Lei Yang, Jian Huang, Jingyu Zhang, and Bin Xiang. Controllable synthesis of high quality monolayer WS₂ on a SiO₂/si substrate by chemical vapor deposition. *RSC Advances*, 5(21):15795–15799, 2015.

- [8] Yang Gao, Zhibo Liu, Dong-Ming Sun, Le Huang, Lai-Peng Ma, Li-Chang Yin, Teng Ma, Zhiyong Zhang, Xiu-Liang Ma, Lian-Mao Peng, Hui-Ming Cheng, and Wencai Ren. Large-area synthesis of high-quality and uniform monolayer WS₂ on reusable Au foils. *Nature Communications*, 6(1), oct 2015.
- [9] Yongji Gong, Junhao Lin, Xingli Wang, Gang Shi, Sidong Lei, Zhong Lin, Xiaolong Zou, Gonglan Ye, Robert Vajtai, Boris I. Yakobson, Humberto Terrones, Mauricio Terrones, Beng Kang Tay, Jun Lou, Sokrates T. Pantelides, Zheng Liu, Wu Zhou, and Pulickel M. Ajayan. Vertical and in-plane heterostructures from WS₂/MoS₂ monolayers. *Nature Materials*, 13(12):1135–1142, sep 2014.
- [10] Yongji Gong, Zhong Lin, Gonglan Ye, Gang Shi, Simin Feng, Yu Lei, Ana Laura Elías, Nestor Perea-Lopez, Robert Vajtai, Humberto Terrones, Zheng Liu, Mauricio Terrones, and Pulickel M. Ajayan. Tellurium-assisted low-temperature synthesis of MoS₂ and WS₂ monolayers. *ACS Nano*, 9(12):11658–11666, nov 2015.
- [11] Humberto R. Gutiérrez, Nestor Perea-López, Ana Laura Elías, Ayse Berkdemir, Bei Wang, Ruitao Lv, Florentino López-Urías, Vincent H. Crespi, Humberto Terrones, and Mauricio Terrones. Extraordinary room-temperature photoluminescence in triangular ws₂ monolayers. *Nano Letters*, 13(8):3447–3454, dec 2013. PMID: 23194096.
- [12] Wolfgang K. Hofmann. Thin films of molybdenum and tungsten disulphides by metal organic chemical vapour deposition. *Journal of Materials Science*, 23(11):3981–3986, nov 1988.
- [13] Wang Yao Di Xiao Hualing Zeng, Junfeng Dai and Xiaodong Cui. Valley polarization in mos₂ monolayers by optical pumping. *Nature Nanotechnology*, 7(8):490–493, jun 2012.
- [14] M Waqas Iqbal, M Zahir Iqbal, M Farooq Khan, M Arslan Shehzad, Yongho Seo, Jong Hyun Park, Chanyong Hwang, and Jonghwa Eom. High-mobility and air-stable single-layer WS₂ field-effect transistors sandwiched between chemical vapor deposition-grown hexagonal BN films. *Scientific Reports*, 5(1), jun 2015.
- [15] Sanghyun Jo, Nicolas Ubrig, Helmuth Berger, Alexey B. Kuzmenko, and Alberto F. Morpurgo. Mono- and bilayer ws₂ light-emitting transistors. *Nano Letters*, 14(4):2019–2025, 2014. PMID: 24669957.
- [16] Kibum Kang, Saïen Xie, Lujie Huang, Yimo Han, Pinshane Y. Huang, Kin Fai Mak, Cheol-Joo Kim, David Muller, and Jiwoong Park. High-mobility three-atom-thick semiconducting films with wafer-scale homogeneity. *Nature*, 520(7549):656–660, apr 2015.
- [17] A. Kuc, N. Zibouche, and T. Heine. Influence of quantum confinement on the electronic structure of the transition metal sulfide *ts*₂. *Phys. Rev. B*, 83(24):245213, Jun 2011.
- [18] Yi-Hsien Lee, Lili Yu, Han Wang, Wenjing Fang, Xi Ling, Yumeng Shi, Cheng-Te Lin, Jing-Kai Huang, Mu-Tung Chang, Chia-Seng Chang, Mildred Dresselhaus, Tomas Palacios, Lain-Jong Li, and Jing Kong. Synthesis and transfer of single-layer transition metal disulfides on diverse surfaces. *Nano Letters*, 13(4):1852–1857, mar 2013.
- [19] Shisheng Li, Shunfeng Wang, Dai-Ming Tang, Weijie Zhao, Huilong Xu, Lei Qiang Chu, Yoshio Bando, Dmitri Golberg, and Goki Eda. Halide-assisted atmospheric pressure growth of large WSe₂ and WS₂ monolayer crystals. *Applied Materials Today*, 1(1):60–66, nov 2015.

- [20] Tianshu Li and Giulia Galli. Electronic properties of mos2 nanoparticles. *The Journal of Physical Chemistry C*, 111(44):16192–16196, nov 2007.
- [21] Yilei Li, Yi Rao, Kin Fai Mak, Yumeng You, Shuyuan Wang, Cory R. Dean, and Tony F. Heinz. Probing symmetry properties of few-layer mos2 and h-bn by optical second-harmonic generation. *Nano Letters*, 13(7):3329–3333, jun 2013. PMID: 23718906.
- [22] Liangxu Lin, Yaoxian Xu, Shaowei Zhang, Ian M. Ross, Albert C. M. Ong, and Dan A. Allwood. Fabrication of luminescent monolayered tungsten dichalcogenides quantum dots with giant spin-valley coupling. *ACS Nano*, 7(9):8214–8223, 2013. PMID: 23968363.
- [23] He Keliang Lee Changgu Lee Gwan Hyoung Hone James Heinz Tony F. Mak, Kin Fai and Jie Shan. Tightly bound trions in monolayer. *Nature Materials*, 12(3):207–211, dec 2013.
- [24] He Keliang Shan Jie Mak, Kin Fai and Tony F. Heinz. Control of valley polarization in monolayer mos2 by optical helicity. *Nature Nanotechnology*, 7(8):494–498, jun 2012.
- [25] Kin Fai Mak, Changgu Lee, James Hone, Jie Shan, and Tony F. Heinz. Atomically thin mos_2 : A new direct-gap semiconductor. *Phys. Rev. Lett.*, 105(13):136805, Sep 2010.
- [26] Mitsuhiro Okada, Takumi Sawazaki, Kenji Watanabe, Takashi Taniguchi, Hiroki Hibino, Hisanori Shinohara, and Ryo Kitaura. Direct chemical vapor deposition growth of ws2 atomic layers on hexagonal boron nitride. *ACS Nano*, 8(8):8273–8277, 2014. PMID: 25093606.
- [27] Namphung Peimyoo, Jingzhi Shang, Chunxiao Cong, Xiaonan Shen, Xiangyang Wu, Edwin K. L. Yeow, and Ting Yu. Nonblinking, intense two-dimensional light emitter: Monolayer ws2 triangles. *ACS Nano*, 7(12):10985–10994, 2013. PMID: 24266716.
- [28] Youmin Rong, Ye Fan, Ai Leen Koh, Alex W. Robertson, Kuang He, Shanshan Wang, Haijie Tan, Robert Sinclair, and Jamie H. Warner. Controlling sulphur precursor addition for large single crystal domains of WS2. *Nanoscale*, 6(20):12096–12103, sep 2014.
- [29] Jingzhi Shang, Xiaonan Shen, Chunxiao Cong, Namphung Peimyoo, Bingchen Cao, Mustafa Eginligil, and Ting Yu. Observation of excitonic fine structure in a 2d transition-metal dichalcogenide semiconductor. *ACS Nano*, 9(1):647–655, 2015. PMID: 25560634.
- [30] Andrea Splendiani, Liang Sun, Yuanbo Zhang, Tianshu Li, Jonghwan Kim, Chi-Yung Chim, Giulia Galli, and Feng Wang. Emerging photoluminescence in monolayer mos2. *Nano Letters*, 10(4):1271–1275, apr 2010. PMID: 20229981.
- [31] Xiaona Liu Pingheng Tan Tengfei Yan, Xiaofen Qiao and Xinhui Zhang. Photoluminescence properties and exciton dynamics in monolayer wse2. *Applied Physics Letters*, 105(10):101901, sep 2014.
- [32] Qing Hua Wang, Kourosh Kalantar-Zadeh, Andras Kis, Jonathan N. Coleman, and Michael S. Strano. Electronics and optoelectronics of two-dimensional transition metal dichalcogenides. *Nature Nanotechnology*, 7:699 EP –, Nov 2012. Review Article.
- [33] Kiran Kumar Amara Jing Ren Pang Minglin Toh Xin Zhang Christian Kloc Ping Heng Tane Weijie Zhao, Zohreh Ghorannevis and Goki Eda. Lattice dynamics in mono- and few-layer sheets of ws_2 and wse_2 . *Nanoscale*, 5(20):9677-9683, August 2013.

- [34] J.A. Wilson and A.D. Yoffe. The transition metal dichalcogenides discussion and interpretation of the observed optical, electrical and structural properties. *Advances in Physics*, 18(73):193–335, may 1969.
- [35] F. Withers, O. Del Pozo-Zamudio, A. Mishchenko, A. P. Rooney, A. Gholinia, K. Watanabe, T. Taniguchi, S. J. Haigh, A. K. Geim, A. I. Tartakovskii, and K. S. Novoselov. Light-emitting diodes by band-structure engineering in van der waals heterostructures. *Nature Materials*, 14(3):301–306, feb 2015.
- [36] Di Xiao, Gui-Bin Liu, Wanxiang Feng, Xiaodong Xu, and Wang Yao. Coupled spin and valley physics in monolayers of mos_2 and other group-vi dichalcogenides. *Phys. Rev. Lett.*, 108(19):196802, May 2012.
- [37] Zai-Quan Xu, Yupeng Zhang, Shenghuang Lin, Changxi Zheng, Yu Lin Zhong, Xue Xia, Zhipeng Li, Ponraj Joice Sophia, Michael S. Fuhrer, Yi-Bing Cheng, and Qiaoliang Bao. Synthesis and transfer of large-area monolayer ws_2 crystals: Moving toward the recyclable use of sapphire substrates. *ACS Nano*, 9(6):6178–6187, 2015. PMID: 25961515.
- [38] Long Yuan and Libai Huang. Exciton dynamics and annihilation in WS_2 2d semiconductors. *Nanoscale*, 7(16):7402–7408, 2015.
- [39] Seok Joon Yun, Sang Hoon Chae, Hyun Kim, Jin Cheol Park, Ji-Hoon Park, Gang Hee Han, Joo Song Lee, Soo Min Kim, Hye Min Oh, Jinbong Seok, Mun Seok Jeong, Ki Kang Kim, and Young Hee Lee. Synthesis of centimeter-scale monolayer tungsten disulfide film on gold foils. *ACS Nano*, 9(5):5510–5519, apr 2015.
- [40] Longhui Zeng, Lili Tao, Chunyin Tang, Bo Zhou, Hui Long, Yang Chai, Shu Ping Lau, and Yuen Hong Tsang. High-responsivity UV-vis photodetector based on transferable WS_2 film deposited by magnetron sputtering. *Scientific Reports*, 6(1), jan 2016.
- [41] Yu Zhang, Yanfeng Zhang, Qingqing Ji, Jing Ju, Hongtao Yuan, Jianping Shi, Teng Gao, Donglin Ma, Mengxi Liu, Yubin Chen, Xiuju Song, Harold Y. Hwang, Yi Cui, and Zhongfan Liu. Controlled growth of high-quality monolayer ws_2 layers on sapphire and imaging its grain boundary. *ACS Nano*, 7(10):8963–8971, 2013. PMID: 24047054.
- [42] Weijie Zhao, Zohreh Ghorannevis, Leiqiang Chu, Minglin Toh, Christian Kloc, Ping-Heng Tan, and Goki Eda. Evolution of electronic structure in atomically thin sheets of ws_2 and wse_2 . *ACS Nano*, 7(1):791–797, dec 2013. PMID: 23256505.
- [43] Z. Y. Zhu, Y. C. Cheng, and U. Schwingenschlögl. Giant spin-orbit-induced spin splitting in two-dimensional transition-metal dichalcogenide semiconductors. *Phys. Rev. B*, 84(15):153402, Oct 2011.